Optical Materials 99 (2020) 109589

Contents lists available at ScienceDirect

Optical Materials

journal homepage: http://www.elsevier.com/locate/optmat

Fabrication and photocatalytic property of MoO_x nano-particle films from Mo target by laser ablation at ambient conditions

Ruijin Hong [a], Zhengwang Li [a], Qingyou Liu [b], Wenfeng Sun [a], Cao Deng [a], Qi Wang [a], Hui Lin [a], Chunxian Tao [a], Dawei Zhang [a,*]

[a] Engineering Research Center of Optical Instrument and System, Ministry of Education and Shanghai Key Lab of Modern Optical System, University of Shanghai for Science and Technology, No.516 Jungong Road, Shanghai, 200093, China
[b] Key Laboratory of High-temperature and High-pressure Study of the Earth's Interior, Institute of Geochemistry, Chinese Academy of Sciences, Guiyang, 550081, China

ARTICLE INFO

Keywords:
MoO_x NP films
Laser ablation
Laser irradiation
Photocatalytic
Oxygen vacancies
LSPR

ABSTRACT

MoO_x nanoparticle (NP) films were fabricated through laser ablation from molybdenum target at ambient conditions. The structure, optical properties and photocatalytic performance of the MoO_x NP films were characterized under different laser irradiation times. XRD patterns indicate that laser irradiation can accelerate the oxidation and improve the orientation of MoO_x NP films. The samples after irradiation show broad absorption peaks from the visible to infrared regions with significant improvement photocatalytic performance in hydrogen generation compared with that of the as-ablated sample with 1.33 times. The oxygen vacancies generated in the case of laser irradiation was demonstrated to dominate the localized surface plasmon resonance (LSPR) and photocatalytic performance by varying the laser irradiation times.

1. Introduction

With the increase in global energy consumption, it is necessary to develop clean energy. Hydrogen, a pollution-free energy, has attracted worldwide attention. The decomposition of water to produce hydrogen with photocatalyst and UV light is considered as an effective method [1]. It is reported that, noble metal NPs supported on carbon have been utilized to promote photocatalytic hydrogen evolution [2]. However, their future developments are constrained by the high cost. In recent years, some low-cost metal oxides have shown good photocatalytic properties, such as TiO_2 [1], WO_{3-x} [3], MoO_{3-x} [4] and so on.

Molybdenum trioxide (MoO_3), an excellent semiconducting material with a wide energy band gap (3.2eV) [5], has been widely used in gas sensing [6], catalysis [7,8] and others. MoO_3 NPs can be prepared by salt-templated [9], hydrothermal synthesis [10] and so on. However, these methods are not only complicated but also environmentally harmful. Besides, MoO_3 has poor photocatalytic properties due to its wide band gap and high recombination of photo-generated electron--hole pairs [11]. Therefore, oxygen defect engineering has been introduced to modify the properties of MoO_3, narrowing the band gap and increasing the lifetime of electron-hole pairs [12–14]. Actually, a large number of electrons are adsorbed around the oxygen vacancies [15], which will not only lead to surface plasmon resonance, but also increase hydrogen production. Various methods are put forward to introduce oxygen vacancies, such as ball milling [16], hydrogen treatment [17,18] and air annealing [19,20]. Nevertheless, these methods are complex and inefficient.

Laser ablation/irradiation is a green technique for obtaining nanoparticles of metal oxides, semiconductors and so on [21]. Herein, the oxygen-deficient MoO_x NP films were synthesized through fairly simple programs of laser ablation and irradiation. The photocatalytic performance of MoO_x NP films was easily tuned by varying the irradiation times. The structure and morphology were studied by X-ray diffraction (XRD) along with atomic force microscopy (AFM). The compositions of the as-prepared MoO_x film were determined by Raman spectroscopy coupled with X-ray photoelectron spectroscopy (XPS). The phenomenon of LSPR of MoO_x NP films were revealed through UV-VIS-NIR double beam spectrometer. The electric field distribution of MoO_x nanospheres was calculated by Finite-Difference Time-Domain (FDTD).

* Corresponding author.
E-mail address: dwzhang@usst.edu.cn (D. Zhang).

https://doi.org/10.1016/j.optmat.2019.109589
Received 23 September 2019; Received in revised form 19 November 2019; Accepted 28 November 2019
Available online 10 December 2019

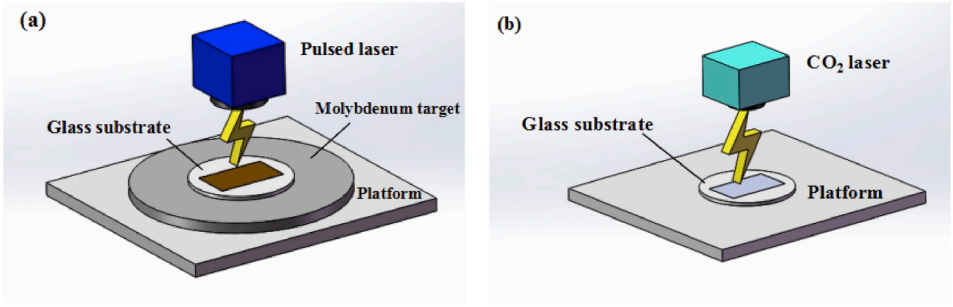

Fig. 1. The schematic diagram of (a) laser ablation and (b) laser irradiation.

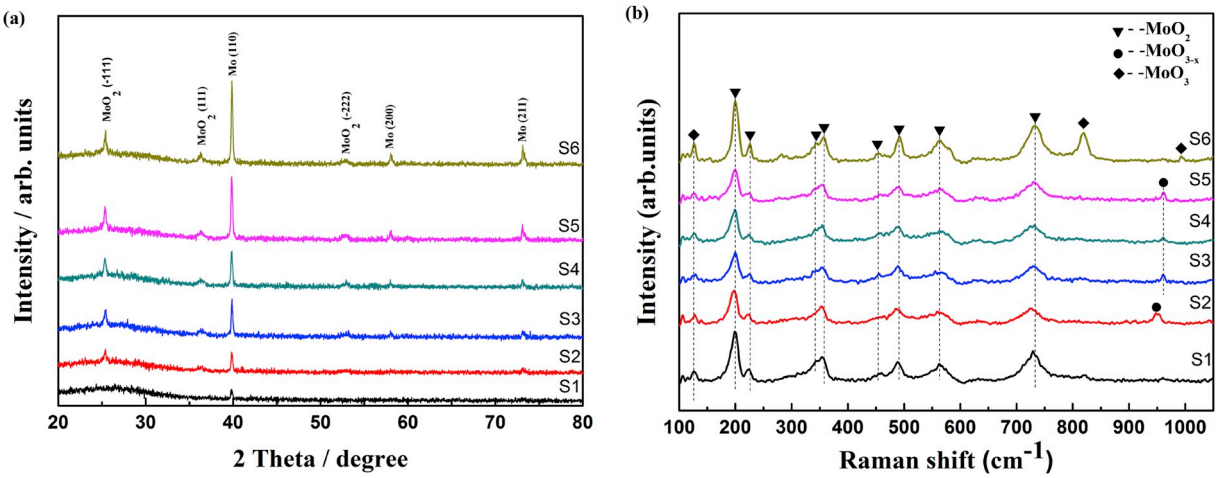

Fig. 2. (a) The XRD patterns of samples before and after laser irradiation; (b) the Raman spectra of samples before and after laser irradiation.

2. Experiment

2.1. Preparation and sample characterization

MoO_x NP film with the area of 12 × 12 mm were obtained by Nd: YAG pulsed laser (λ = 1064 nm) ablation using a molybdenum target (99.99%) under ambient conditions. Parameters of the pulsed laser beam were as follows: the laser beam power was 4.6 W, the scan speed was 300 mm/s, the pulse width was 9 ns, the beam diameter and scanning line spacing were 0.01 mm. Then, these MoO_x NP films would be irradiated by CO_2 laser (λ = 10.6 μm). Parameters of CO_2 laser were as follows: laser power was 2 W, the scan speed was set at 40 mm/s. The as-ablated film was marked as S1, and the as-irradiated films which were irradiated for 1, 3, 5, 7 and 9 times, were marked as S2–S6, respectively. Fig. 1 shows the schematic diagram of the procedure.

The phases of the samples were studied by XRD (MiniFlex600 system, Rigaku). Raman signals were obtained by the Renishaw Raman spectroscopy with 633 nm laser excitation. A surface analysis of the samples was conducted by the Thermo Scientific K-Alpha + X-ray photoelectron spectroscopy (XPS). The surface morphology was analyzed through AFM (XE-100, Park System). The absorption spectra were characterized by a Perkins Elmer UV–Vis–NIR spectrophotometer.

2.2. Photocatalytic reaction

The photocatalytic reaction was carried out in a home-made photocatalytic evaluation system (CEL-SPH2N, Beijing). The light source was a 300 W xenon lamp (CEL-HXF 300) with a 420 nm UV band-pass filter. MoO_x NP film worked as a photocatalyst and was placed in a glass container with 50 mL deionized water. The distance between sample and light source was 10 cm, and the intensity of the irradiation was 90×10^3 Lux. The photocatalytic reaction temperature was set 6 °C and maintained with a cooling-water jacket. Before irradiation, we used a vacuum pump to remove the air and dissolved oxygen completely, making the base vacuum less than 0.1 MPa. The photocatalytic activity was analyzed every half an hour and 3 mL gas was extracted into a chromatograph equipped with nitrogen as carrier gas.

3. Results and discussion

3.1. Crystal structure

The effect of laser irradiation time on the crystal structure of the as-ablated film is revealed in Fig. 2(a). The as-ablated sample shows relatively poor crystallinity with the only peak located at 39.8° (2θ), corresponding to (110) of Mo (JCPDS No. 89–5023). It indicates the grain orientation of Mo is preferred along the direction of (110) crystal owing to the lowest surface energy. Once irradiated, the XRD patterns of the as-irradiated films show several new peaks: 25.4° (2θ), 36.26° (2θ), 52.94° (2θ) correspond to the (−111), (111), (−222) of MoO_2 (JCPDS No. 76–1807) and 57.98° (2θ), 73.12° (2θ) correspond to the (200) and (211) of Mo (JCPDS No. 89–5023), respectively. With the increase of irradiation time, these as-irradiated samples exhibit narrower and stronger peaks compared with the as-ablated sample, meaning the laser irradiation improved the crystallinity since the thermal treatment can restore structure defects [22–24]. In addition, laser irradiation accelerates the oxidation of Mo.

Fig. 2(b) shows the Raman spectra of the samples before and after laser irradiation. The spectrum of the as-ablated sample consists of the following peaks: 200, 226, 344, 358, 452, 491, 563, and 733 cm^{-1}. These peaks are consistent well with the lattice vibration modes of monoclinic MoO_2 phase (m-MoO_2) [25]. Among them, the Raman bands

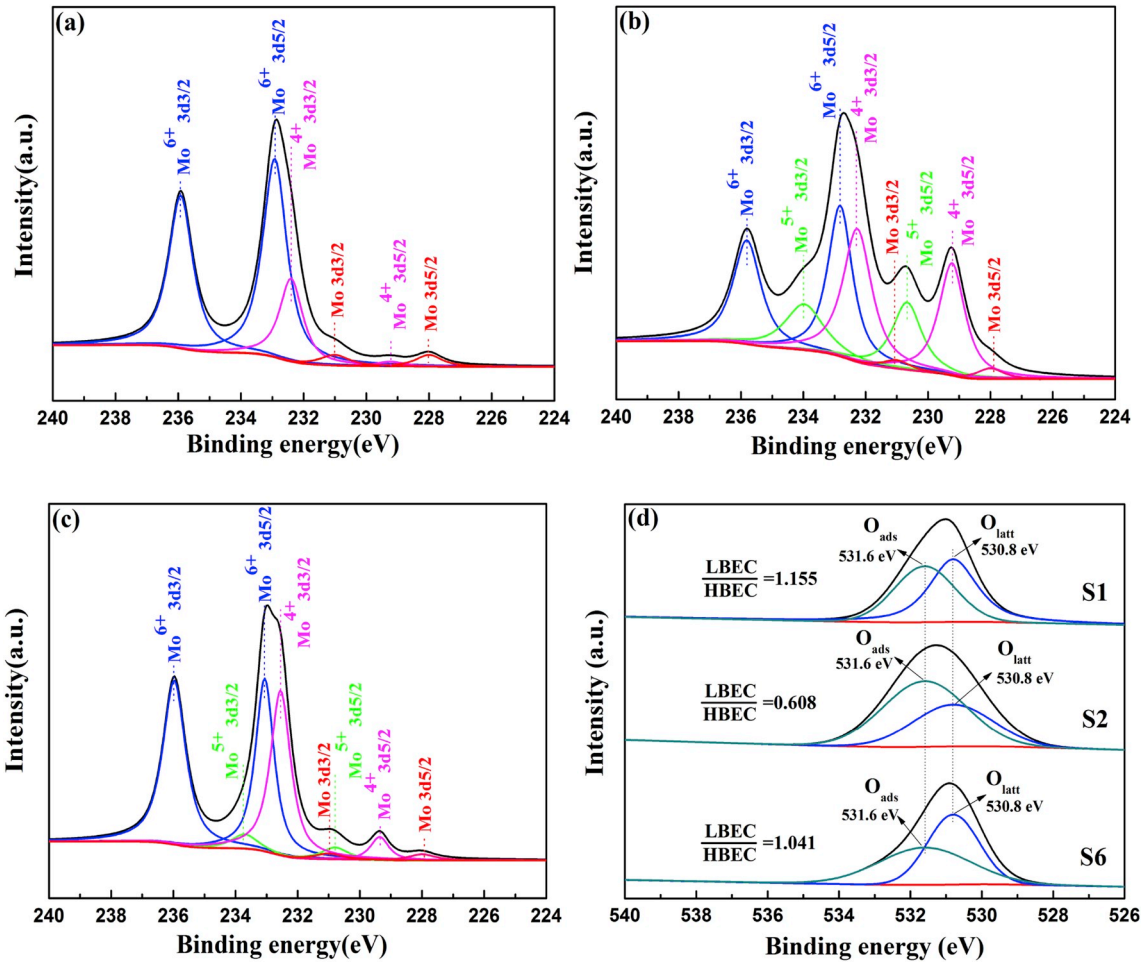

Fig. 3. The XPS spectra of MoO_x in the Mo 3d region from (a) S1, (b) S2 and (c) S6; (d) the XPS spectra of O 1s of S1, S2 and S6.

at 563 and 733 cm^{-1} are caused by the stretching vibration of the O–Mo–O and Mo═O bonds [26]. Raman peaks locate at 127 cm^{-1}, corresponding unambiguously to the MoO_3 [27]. For the as-irradiated samples (S2–S5), peaks appear around 950 cm^{-1} and 961 cm^{-1}, which are related to the MoO_{3-x} crystalline phase [28]. The observed frequency shift is caused by the non-harmonic effect [29]. When the sample is irradiated for 9 times, two new peaks around 819 cm^{-1} (corner-sharing O–Mo–O) and 993 cm^{-1} (M = O) [30] are also corresponding to the MoO_3. Especially, the presence of the peak locates at 993 cm^{-1}, corresponding to the tensile vibration of Mo-based (Mo═O) units, and these units are merely exist in the α-MoO_3 phase [27]. Raman spectra show that the increase of irradiation times leading to the oxidation degree deepens, and then MoO_{3-x} will transform to MoO_3. Generally, S1 is composed of MoO_2 and MoO_3, the others are composed of MoO_2, MoO_{3-x} ($0 < x < 1$) and MoO_3. Combining with the XRD diagram, it can be proved that Mo is present in all samples. With irradiation time increasing, part of Mo NPs continue to react with oxygen to form MoO_2, MoO_{3-x} and MoO_3, MoO_2 will further react with oxygen to produce MoO_{3-x} and MoO_3. No obvious peaks corresponding to those of MoO_{3-x} and MoO_3 in XRD spectra, indicating that the crystallinity of these two substances is poor.

3.2. Composition and valence state

Fig. 3(a)-(c) shows the representative XPS spectra of samples before and after laser irradiation with different times. Fig. 3(a) shows the XPS spectrum of the as-ablated sample. The doublets at 235.84 and 232.94 eV are ascribed to the binding energies of the $3d_{3/2}$ and $3d_{5/2}$ orbital electrons of Mo^{6+}, respectively. Besides, another two peaks center at 232.41 and 229.21 eV correspond to $3d_{3/2}$ and $3d_{5/2}$ of Mo^{4+} [31]. The doublets at 231 and 228 eV correspond to $3d_{3/2}$ and $3d_{5/2}$ of Mo [32]. Fig. 3(b) shows the XPS spectrum of S2 that was irradiated once. After laser irradiation, a new set of doublets appeared at 233.96 and 230.71 eV corresponding to Mo^{5+} [31]. Moreover, Mo^{6+}, Mo^{4+}, and Mo also exist in the sample while the content has changed, which is attributed to the oxidation of laser irradiation. With the increased irradiation time, the content of Mo^{4+}, Mo^{5+}, and Mo decreased while Mo^{6+} increased. Because more oxygen involved in the reaction. The relative ratios of molybdenum components with different oxidation states are tabulated in Table 1. As discussed above, when the sample is irradiated by CO_2 laser, the sub-stoichiometry MoO_{3-x} will be formed. Besides, the content of MoO_{3-x} will decrease with the increase of irradiation times. Fig. 3(d) is the O 1s spectra peaks of the three samples. The binding energy at 530.8 eV and 531.6 eV correspond to the lattice oxygen (O_{latt}) known as low binding energy peak (LBEC) and the adsorbed oxygen (O_{ads}) assigned as high binding energy peak (HBEC), respectively [33]. The increase of oxygen vacancy will lead to the increase of HBEC components, and may

Table 1
Relative ratio of molybdenum components with different oxidation states calculated from the XPS of Mo 3d Spectra.

	Mo^{6+}(%)	Mo^{5+}(%)	Mo^{4+}(%)	Mo(%)
S1	76.3%	0	18.2%	5.5%
S2	37.6%	21.1%	38.5%	2.8%
S6	59.5%	5.8%	32.1%	2.6%

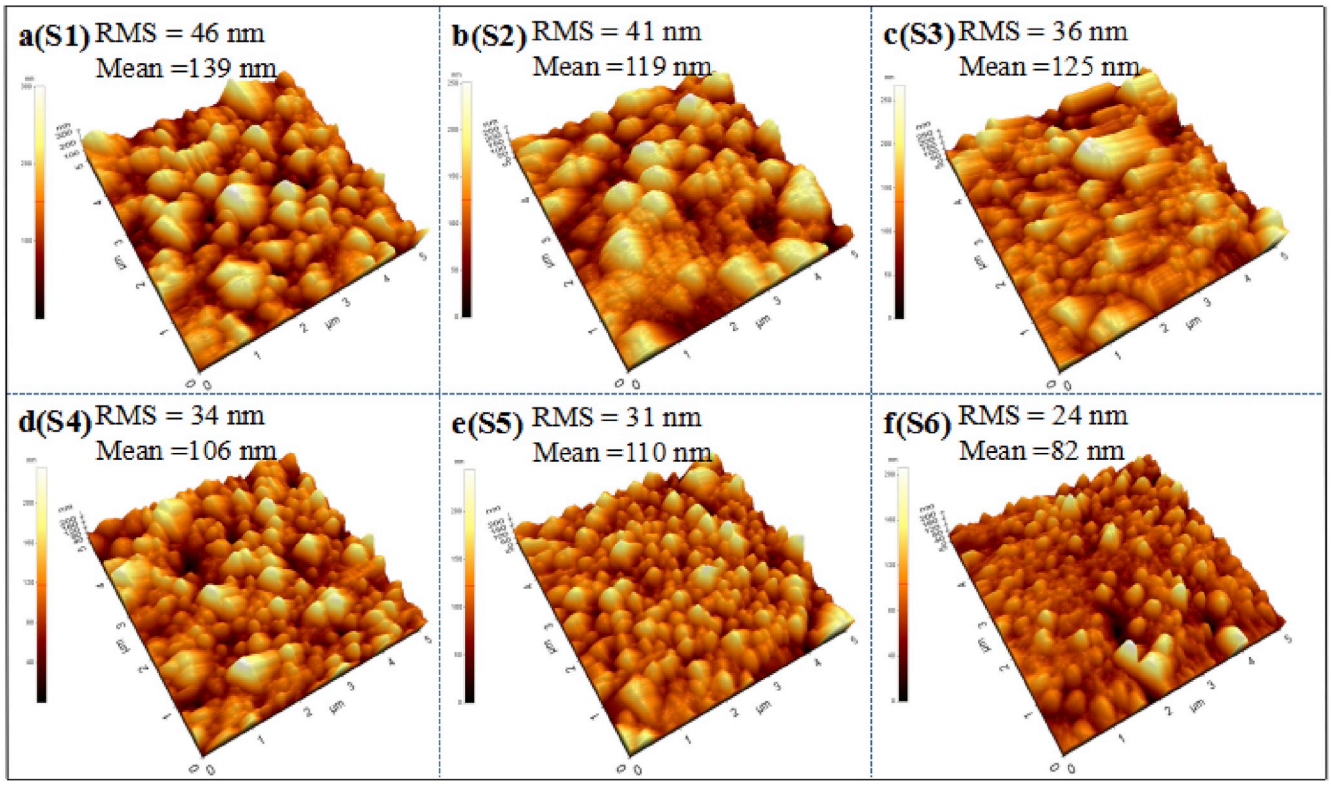

Fig. 4. The AFM images of samples before and after laser irradiation.

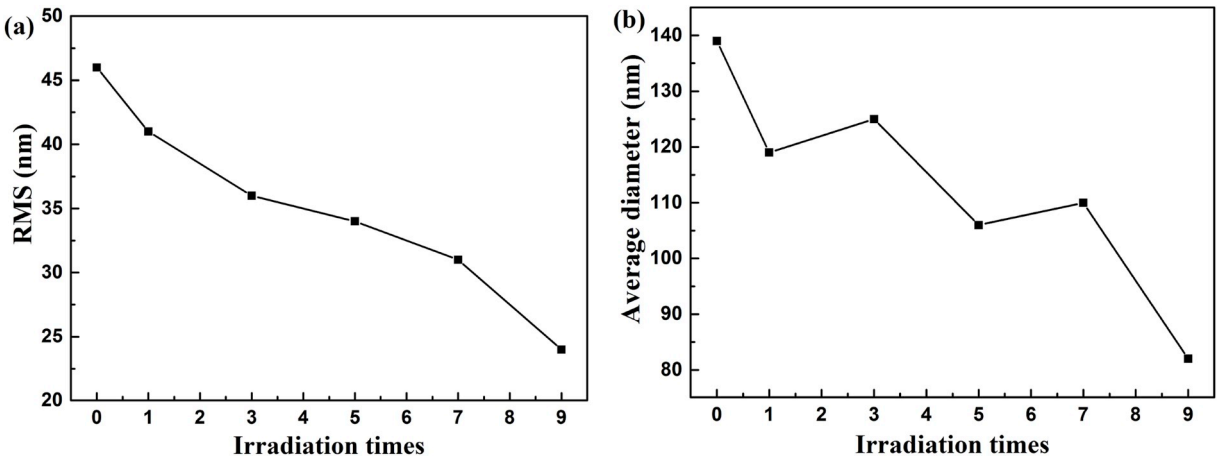

Fig. 5. (a) The surface roughness of samples as a function of irradiation times; (b) the average diameter of samples as a function of irradiation times.

cause the asymmetry of the main peak [34]. In our samples, the ratios of lattice oxygen to adsorbed oxygen to are 1.155, 0.608, and 1.041 for the as-prepared S1, S2, and S6, respectively, which strongly indicate that there are massive oxygen deficiencies in S2. The reasons for the inconsistency between XPS and XRD are as follows: first, the crystallinity of MoO_2 and MoO_3 in the as-ablated sample is poor, so there is no corresponding diffraction peak in XRD. Second, when the as-ablated sample was modified by laser irradiation, the crystallinity of Mo and MoO_2 was improved, but that of MoO_{3-x} and MoO_3 were not. Those fitting results demonstrate that laser irradiation will vary the oxygen vacancies concentration and change the composition of MoO_x.

3.3. Surface morphology

The AFM images for the as-ablated sample and as-irradiated samples are displayed in Fig. 4. The nanoparticle size of as-ablated sample is larger, the height distribution is wide, and the valley is lower. After laser irradiation, it develops from rough and accumulated island structures into small and sharp islands. Meanwhile, the surface of as-irradiated MoO_x NP films becomes relatively smooth and the surface roughness values (Rq) are 55.59, 40.9, 35.6, 34.38, 31.32 and 24.27 nm, respectively, as is shown in Fig. 5(a). In addition, it can be seen from Fig. 5(b), with the increase of irradiation times, the size of nanoparticles fluctuates to some extent, but on the whole, the size of nanoparticles decreases.

Apparently, laser irradiation plays an important role in changing the morphology of samples. The laser energy is transferred to MoO_x NP films, causing the films to melt. Then instability of the large size nanoparticles transformed into smaller nanoparticles [35–37]. Moreover, since there are phase transformations, that this is the reason for the observed trend of decreasing particle size with the irradiation.

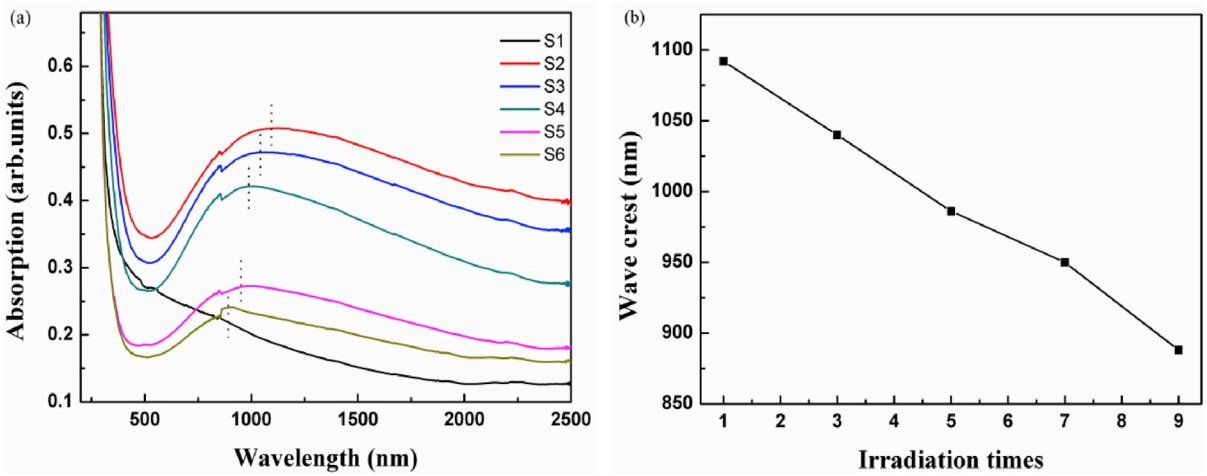

Fig. 6. (a) Absorption spectra of samples before and after laser irradiation; (b) curve of wave crests from every absorption spectrum.

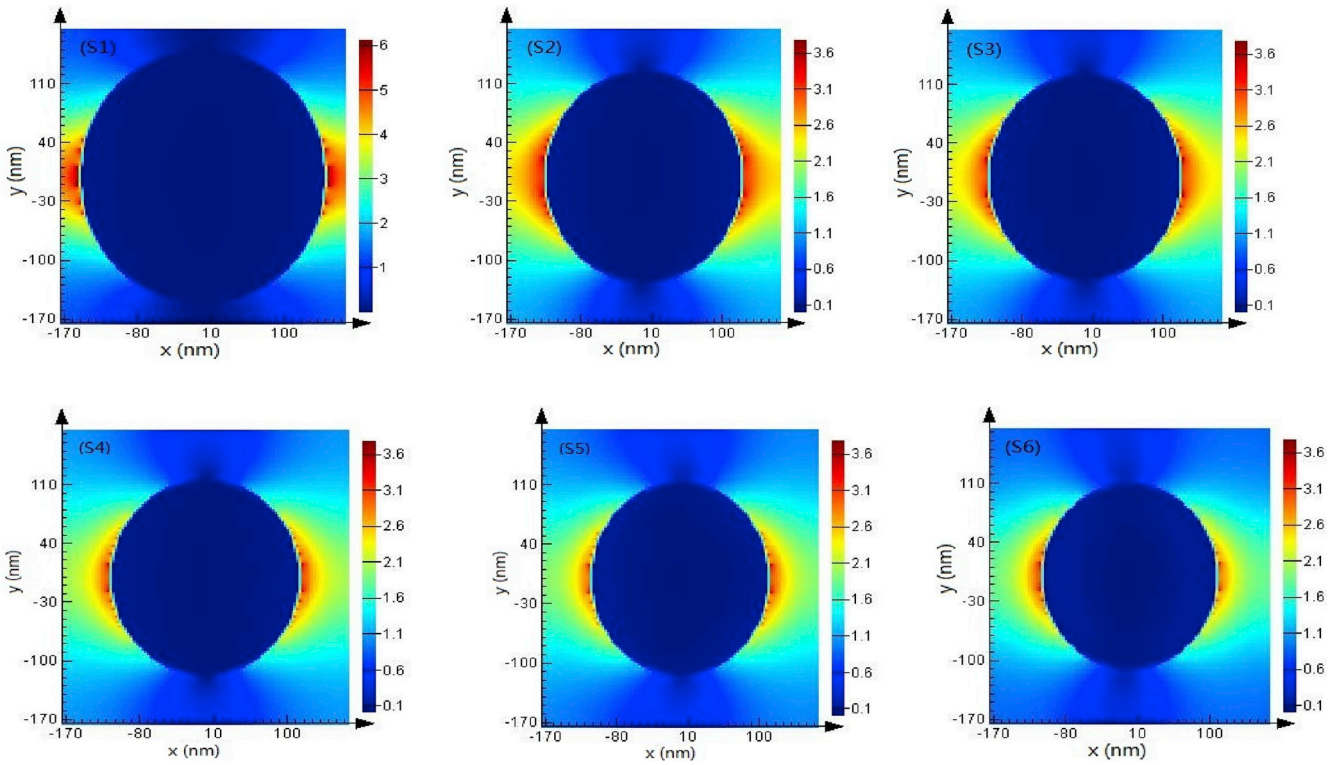

Fig. 7. The FDTD simulated electric field amplitude patterns of samples before and after laser irradiation.

3.4. Optical absorption

Fig. 6(a) shows the absorption spectra of samples before and after laser irradiation. There is no plasma absorption peak in the as-ablated sample. While broad absorption peaks appear in the near-infrared (NIR) region for those as-irradiated samples. With the increase of irradiation times, a blue-shift of LSPR peak is shown from 1092 nm to 888 nm with the intensity of LSPR decreasing gradually. According to Fig. 6 (b), there is a wave crest represents the maximum absorption wavelength of each absorption spectrum, and the peaks locate at 1092, 1040, 986, 950 and 888 nm, respectively.

Those LSPR absorption peaks may be attributed to its very high concentration oxygen vacancies contained in the MoO_{3-x} NPs, a large number of electrons are adsorbed around the oxygen vacancies and then cause LSPR [15]. With the increase of irradiation times, oxidation reaction will reduce the content of oxygen vacancies so that the intensity of LSPR decreases [38]. The size and shape of the NPs affect the wavelength of plasma, which is a quasi-static theory for calculating the absorption of NPs with ellipsoid structure [39]. Therefore, due to the decrease of the size of MoO_x NPs, the wavelength of LSPR shifts blue, which is consistent with the AFM diagram.

To further explore whether particle size will cause LSPR, the electric field distribution is simulated by FDTD. The polarized 633 nm laser along the y-axis irradiates vertically to the x-y plane of the samples. Fig. 7 shows the electric field intensity of MoO_x under different irradiation times. The results show that the smaller the size of nanoparticles is, the smaller the electric field intensity is. Physically, LSPR is a response to the electric field of incident light, so it often leads to a significant enhancement of the electric field near nanoparticles [40]. Therefore, maybe we can explain Fig. 6(S2–S6) in terms of particle size. The small

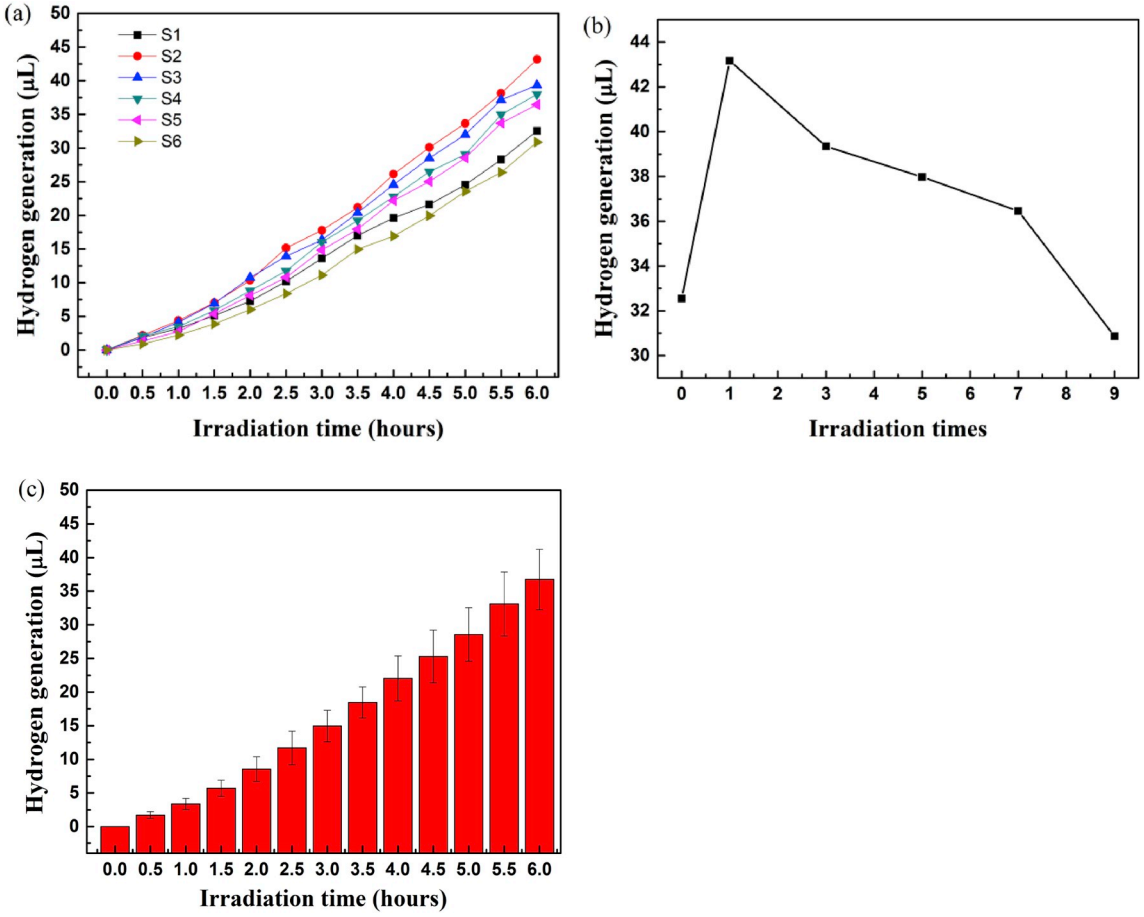

Fig. 8. (a) The photocatalytic performance of samples before and after laser irradiation; (b) the relationship between irradiation times and hydrogen yield; (c) the errors bars of hydrogen generation as a function of irradiation times.

particle size would decrease the electric field intensity around the particle, and the LSPR peak intensity weakened too. It is worth noting that S1 with the largest size had the strongest electric field intensity, but it do not show LSPR phenomenon. Therefore, the LSPR of these samples are caused by oxygen vacancies rather than the surface morphology of MoO_x NP films.

3.5. Photocatalysis

In order to explore the photocatalytic property of MoO_x NP films, we evaluated these samples under UV light irradiation for 6 h through the photocatalytic evaluation system. As shown in Fig. 8(a), the hydrogen yield of S1 is 32.55 μL. For the as-irradiated samples, with the irradiation time increasing, their hydrogen yields are 43.17, 39.35, 37.97, 36.46 and 30.89 μL, respectively. The H_2 generation for different irradiation times is calculated (Fig. 8(b)), and Fig. 8(c) is the errors bars of hydrogen generation as a function of irradiation times, which indicates the variation of hydrogen production among samples becomes larger with the increase of reaction time.

The as-ablated sample is composed of Mo, MoO_2 and MoO_3. After irradiation, MoO_{3-x} will form. Maximum activity is observed on the as-irradiated sample just for one time. Compared with the as-ablated sample, the photocatalytic activity is significantly improved by introducing the Mo^{5+}. This increase of photocatalytic activity is due to the formation of the oxygen vacancies. The largest yield is almost 1.33 times more than that of the as-ablated sample. However, for S6, the efficiency of photocatalytic decomposition of water is lower than that of as-ablated samples, although the oxygen vacancies also exist in it.

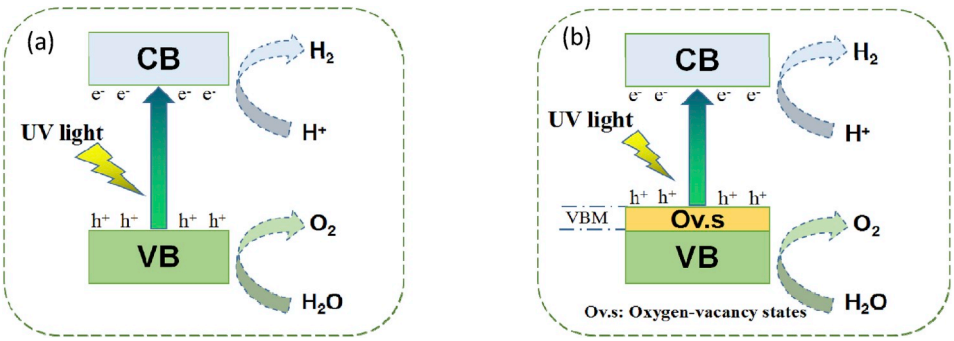

Fig. 9. The mechanism of charge separation and photocatalytic reaction of (a) without and (b) with oxygen vacancies.

Previous research has reported that oxygen vacancies would affect the absorption as well as photocatalytic reactions. Oxygen vacancies play an important role in changing the charge transport, electronic structure, electron/hole separation and surface properties, which would improve the photocatalytic hydrogen evolution [41,42]. When oxygen vacancies are introduced, the quick separation of the photo-generated charges will happen which caused by the raising of valence band maximum (VBM) and expanding of valence band (VB) width [43], as is shown in Fig. 9. Above all, a certain amount of MoO_{3-x} will increase hydrogen production, but it gradually decreases with the irradiation time increasing, which is attributed to the recovery of oxygen vacancies [44].

4. Conclusion

In summary, the influence of laser irradiation on the composition, morphology, crystal quality and optical properties of MoO_x NP films were investigated. XRD, XPS, optical absorption results show that by changing the laser irradiation time, the crystal quality, composition and optical properties of MoO_x NP films can be tuned. The hydrogen generation of the as-irradiated sample (S2) is 1.33 times than that of the as-ablated sample, which indicates that the photocatalytic efficiency of S2 is obviously improved.

Author contributions

Writing - original draft: Zhengwang Li.
Writing - review & editing: Ruijin Hong.
Data curation: Qi Wang & Chunxian Tao.
Formal analysis: Hui Lin.
Investigation: Qingyou Liu.
Project administration: Dawei Zhang.
Software: Wenfeng Sun & Cao Deng.
Supervision: Ruijin Hong.
Validation: Dawei Zhang.

Declaration of competing interest

The authors declare that they have no known competing financial interests or personal relationships that could have appeared to influence the work reported in this paper.

Acknowledgments

This work was supported by the National Natural Science Foundation of China (61775140, 61775141), and Shanghai Foundation for Science and Technology Innovation Action Plan (15441902302, 1714220060).

References

[1] A. Fujishima, K. Honda, Electrochemical photolysis of water at semiconductor electrode, Nature 238 (1972) 37–38.
[2] X. Ning, Y. Li, B. Dong, H. Wang, H. Yu, F. Peng, Y. Yang, Electron transfer dependent catalysis of Pt on N-doped carbon nanotubes: effects of synthesis method on metal-support interaction, J. Catal. 348 (2017) 100–109.
[3] T. Paik, M. Cargnello, T.R. Gordon, S. Zhang, H. Yun, J.D. Lee, H.Y. Woo, S.J. Oh, C.R. Kagan, P. Fornasiero, C.B. Murray, Photocatalytic hydrogen evolution from substoichiometric colloidal WO_{3-x} nanowires, ACS Energy Lett. 3 (8) (2018) 1904–1910.
[4] A.S. Etman, H.N. Abdelhamid, Y. Yuan, L. Wang, X. Zou, J. Sun, Facile water-based strategy for synthesizing MoO_{3-x} nanosheets: efficient visible light photocatalysts for dye degradation, ACS Omega 3 (2) (2018) 2193–2201.
[5] A. Varlec, D. Arčon, S.D. Škapin, M. Remškar, Oxygen deficiency in MoO_3 polycrystalline nanowires and nanotubes, Mater. Chem. Phys. 170 (2016) 154–161.
[6] W.-S. Kim, H.-C. Kim, S.-H. Hong, Gas sensing properties of MoO_3 nanoparticles synthesized by solvothermal method, J. Nanoparticle Res. 12 (5) (2009) 1889–1896.
[7] H. Chang, Q. Wu, T. Zhang, M. Li, X. Sun, J. Li, L. Duan, J. Hao, Design strategies for CeO_2-MoO_3 catalysts for $DeNO_x$ and Hg^0 oxidation in the presence of HCl: the significance of the surface acid-base properties, Environ. Sci. Technol. 49 (20) (2015) 12388–12394.
[8] P.M. Shafi, R. Dhanabal, A. Chithambararaj, S. Velmathi, A.C. Bose, α-MnO_2/h-MoO_3 hybrid material for high performance supercapacitor electrode and photocatalyst, ACS Sustain. Chem. Eng. 5 (6) (2017) 4757–4770.
[9] X. Xiao, H. Song, S. Lin, Y. Zhou, X. Zhan, Z. Hu, Q. Zhang, J. Sun, B. Yang, T. Li, L. Jiao, J. Zhou, J. Tang, Y. Gogotsi, Scalable salt-templated synthesis of two-dimensional transition metal oxides, Nat. Commun. 7 (2016), 11296.
[10] G. Song, J. Hao, C. Liang, T. Liu, M. Gao, L. Cheng, J. Hu, Z. Liu, Degradable molybdenum oxide nanosheets with rapid clearance and efficient tumor homing capabilities as a therapeutic nanoplatform, Angew Chem. Int. Ed. Engl. 55 (6) (2016) 2122–2126.
[11] K.V. Alex, A. Prabhakaran, A.R. Jayakrishnan, K. Kamakshi, J.P.B. Silva, K. C. Sekhar, Charge coupling enhanced photocatalytic activity of BaTiO3/MoO3 heterostructures, ACS Appl. Mater. Interfaces 11 (43) (2019) 40114–40124.
[12] X. Dai, Direct partial oxidation of methane to synthesis gas using oxygen carriers in the absence of gaseous oxygen, Prog. Chem. 21 (7) (2009) 1626–1635.
[13] X. Liu, S.R. Bhatia, Laponite® and Laponite®-PEO hydrogels with enhanced elasticity in phosphate-buffered saline, Polym. Adv. Technol. 26 (7) (2015) 874–879.
[14] H. Yan, C. Zhao, K. Wang, L. Deng, M. Ma, G. Xu, Negative dielectric constant manifested by static electricity, Appl. Phys. Lett. 102 (6) (2013), 062904.
[15] L. Kumari, Y.-R. Ma, C.-C. Tsai, Y.-W. Lin, S.Y. Wu, K.-W. Cheng, Y. Liou, X-ray diffraction and Raman scattering studies on large-area array and nanobranched structure of 1D MoO_2 nanorods, Nanotechnology 18 (11) (2007), 115717.
[16] Y. Zhu, Q. Ling, Y. Liu, H. Wang, Y. Zhu, Photocatalytic performance of $BiPO_4$ nanorods adjusted via defects, Appl. Catal. B Environ. 187 (2016) 204–211.
[17] L. Cheng, Y. Hou, B. Zhang, S. Yang, J.W. Guo, L. Wu, H.G. Yang, Hydrogen-treated commercial WO_3 as an efficient electrocatalyst for triiodide reduction in dye-sensitized solar cells, Chem. Commun. (Camb) 49 (53) (2013) 5945–5947.
[18] G. Wang, H. Wang, Y. Ling, Y. Tang, X. Yang, R.C. Fitzmorris, C. Wang, J.Z. Zhang, Y. Li, Hydrogen-treated TiO_2 nanowire arrays for photoelectrochemical water splitting, Nano Lett. 11 (7) (2011) 3026–3033.
[19] Y. Li, Z. Tang, J. Zhang, Z. Zhang, Defect engineering of air-treated WO_3 and its enhanced visible-light-driven photocatalytic and electrochemical performance, J. Phys. Chem. C 120 (18) (2016) 9750–9763.
[20] J. Gan, X. Lu, J. Wu, S. Xie, T. Zhai, M. Yu, Z. Zhang, Y. Mao, S.C. Wang, Y. Shen, Y. Tong, Oxygen vacancies promoting photoelectrochemical performance of In_2O_3 nanocubes, Sci. Rep. 3 (2013) 1021.
[21] H. Zeng, X.-W. Du, S.C. Singh, S.A. Kulinich, S. Yang, J. He, W. Cai, Nanomaterials via laser ablation/irradiation in liquid: a review, Adv. Funct. Mater. 22 (7) (2012) 1333–1353.
[22] R. Hong, W. Shao, W. Sun, C. Deng, C. Tao, D. Zhang, Laser irradiation induced tunable localized surface plasmon resonance of silver thin film, Opt. Mater. 77 (2018) 198–203.
[23] S. Guha, J. Yang, D.L. Williamson, Y. Lubianiker, J.D. Cohen, A.H. Mahan, Structural, defect, and device behavior of hydrogenated amorphous Si near and above the onset of microcrystallinity, Appl. Phys. Lett. 74 (13) (1999) 1860–1862.
[24] E.W.H. Kan, W.K. Choi, C.C. Leoy, W.K. Chim, D.A. Antoniadis, E.A. Fitzgerald, Effect of annealing profile on defect annihilation, crystallinity and size distribution of germanium nanodots in silicon oxide matrix, Appl. Phys. Lett. 83 (10) (2003) 2058–2060.
[25] H. Wu, X. Zhou, J. Li, X. Li, B. Li, W. Fei, J. Zhou, J. Yin, W. Guo, Ultrathin molybdenum dioxide nanosheets as uniform and reusable surface-enhanced Raman spectroscopy substrates with high sensitivity, Small 14 (37) (2018), 1802276.
[26] L. Kumari, Y.R. Ma, C.C. Tsai, Y.W. Lin, Y. Liou, X-ray diffraction and Raman scattering studies on large-area array and nanobranched structure of 1D MoO_2 nanorods, Nanotechnology 18 (11) (2007), 115717.
[27] L. Seguin, M. Figlarz, R. Cavagnat, J.C. Lassègues, Infrared and Raman spectra of MoO_3 molybdenum trioxides and $MoO_3 \cdot xH_2O$ molybdenum trioxide hydrates, Spectrochim. Acta Part A Molecular & Biomolecular Spectroscopy 51 (8) (1995) 1323–1344.
[28] Q. Huang, S. Hu, J. Zhuang, X. Wang, MoO_{3-x}-Based hybrids with tunable localized surface plasmon resonances: chemical oxidation driving transformation from ultrathin nanosheets to nanotubes, Chemistry 18 (48) (2012) 15283–15287.
[29] M. Balkanski, R.F. Wallis, E. Haro, Anharmonic effects in light scattering due to optical phonons in silicon, Phys. Rev. B 28 (4) (1983) 1928–1934.
[30] G. Wang, J. Ni, H. Wang, L. Gao, High-performance CNT-wired MoO_3 nanobelts for Li-storage application, J. Mater. Chem. 1 (12) (2013) 4112–4118.
[31] H.S. Kim, J.B. Cook, H. Lin, J.S. Ko, S.H. Tolbert, V. Ozolins, B. Dunn, Oxygen vacancies enhance pseudocapacitive charge storage properties of MoO_{3-x}, Nat. Mater. 16 (4) (2017) 454–460.
[32] E. Minni, F. Werfel, Oxygen interaction with Mo(100) studied by XPS, AES and EELS 12 (7) (1988) 385–390.
[33] X.Y. Kong, B.-J. Ng, K.H. Tan, X. Chen, H. Wang, A.R. Mohamed, S.-P. Chai, Simultaneous generation of oxygen vacancies on ultrathin BiOBr nanosheets during visible-light-driven CO2 photoreduction evoked superior activity and long-term stability, Catal. Today 314 (2018) 20–27.
[34] L. Zhang, W. Wang, D. Jiang, E. Gao, S. Sun, Photoreduction of CO2 on BiOCl nanoplates with the assistance of photoinduced oxygen vacancies, Nano Res. 8 (3) (2014) 821–831.
[35] M.A. Camacho-López, L. Escobar-Alarcón, M. Picquart, R. Arroyo, G. Córdoba, E. Haro-Poniatowski, Micro-Raman study of the m-MoO_2 to α-MoO_3 transformation induced by cw-laser irradiation, Opt. Mater. 33 (3) (2011) 480–484.
[36] T.R. Anthony, H.E. Cline, Surface rippling induced by surface-tension gradients during laser surface melting and alloying, J. Appl. Phys. 48 (9) (1977) 3888–3894.

[37] D.C. Emmony, R.P. Howson, L.J. Willis, Laser mirror damage in germanium at 10.6 μm, Appl. Phys. Lett. 23 (11) (1973) 598–600.
[38] K. Manthiram, A.P. Alivisatos, Tunable localized surface plasmon resonances in tungsten oxide nanocrystals, J. Am. Chem. Soc. 134 (9) (2012) 3995–3998.
[39] H. Chen, L. Shao, Q. Li, J. Wang, Gold nanorods and their plasmonic properties, Chem. Soc. Rev. 42 (7) (2013) 2679–2724.
[40] X. Ma, H. Sun, Y. Wang, X. Wu, J. Zhang, Electronic and optical properties of strained noble metals: implications for applications based on LSPR, Nano Energy 53 (2018) 932–939.
[41] X. Pan, M.Q. Yang, X. Fu, N. Zhang, Y.J. Xu, Defective TiO_2 with oxygen vacancies: synthesis, properties and photocatalytic applications, Nanoscale 5 (9) (2013) 3601–3614.
[42] L. Jing, B. Xin, F. Yuan, L. Xue, B. Wang, H. Fu, Effects of surface oxygen vacancies on photophysical and photochemical processes of Zn-doped TiO_2 nanoparticles and their relationships, J. Phys. Chem. B 110 (36) (2006) 17860–17865.
[43] Y. Li, Z. Tang, J. Zhang, Z. Zhang, Enhanced photocatalytic performance of tungsten oxide through tuning exposed facets and introducing oxygen vacancies, J. Alloy. Comp. 708 (2017) 358–366.
[44] Y. Li, Z. Tang, J. Zhang, Z. Zhang, Enhanced photocatalytic performance of tungsten oxide through tuning exposed facets and introducing oxygen vacancies, J. Alloy. Comp. 708 (2017) 358–366.